第 42 卷第 5 期
2023 年 10 月

红 外 与 毫 米 波 学 报
J. Infrared Millim. Waves

Vol. 42, No. 5
October, 2023

文章编号：1001-9014(2023)05-0643-09

DOI:10. 11972/j. issn. 1001-9014. 2023. 05. 009

Numerical simulation of scanning nearfield optical microscopy based on the source dipole model

WU Chang-Lin[1,2], WANG Chang[1,2*], CAO Jun-Cheng[1,2*]

(1. Key Laboratory of Terahertz Solid-State Technology, Shanghai Institute of Microsystem and Information Technology, Chinese Academy of Sciences, Shanghai 200050, China;
2. Center of Materials Science and Optoelectronics Engineering, University of Chinese Academy of Sciences, Beijing 100049, China)

Abstract: Scanning near-field optical microscopy in the infrared and terahertz ranges has attracted much interest in studying objects far below the diffraction limit, particularly in the detection of optical properties of structures on the nanoscale. To further understand the tip-sample interaction, analytical and numerical description of the near fields from the probe is essential. Here, we established and analytically solved a more realistic analytical model based on the real probe shape. Based on the combination of the analytical model and numerical simulation to develop the source dipole model (SDM), a comparison with the new method to full-wave simulation (FWS) results was performed. In simulations combined with the theoretical model, the detection information is obtained directly, and the computational efficiency is improved. Based on simulation results, the antenna effect, tip apex radius influence, and the influence of charge amount are explained. This paper provides a new perspective to further understand the tip-sample junction in optical nanoscopy.

Key words: terahertz, nearfield microscopy, numerical simulation, dipole model, optical properties

基于源偶极子的扫描近场光学显微镜的数值模拟

吴昌林[1,2], 王 长[1,2*], 曹俊诚[1,2*]

(1. 中国科学院上海微系统与信息技术研究所太赫兹固态技术重点实验室,上海 200050;
2. 中国科学院大学材料科学与光电工程中心,北京 100049)

摘要:红外和太赫兹范围内的扫描近场光学显微镜能够突破衍射极限,实现更小的空间分辨率,在纳米尺度结构的光学特性分析检测方面具有重要应用。为了进一步理解探针与样品的相互作用,对探针近场的分析和数值描述是必不可少的。基于真实的探针形状的解析模型,结合数值模拟的开发了源偶极子模型(SDM),能够直接获得近场检测信息,提高计算效率。基于模拟结果,解释了天线效应、尖端半径影响和电荷量的影响,并将SDM模型结果与全波仿真(FWS)结果进行了比较。为进一步理解近场光学显微镜中的针尖-样品结提供了新的视角。

关 键 词:太赫兹;近场显微技术;数值模拟;偶极模型;光学性质

中图分类号:O472+.3 **文献标识码**:A

Introduction

Scanning near-field optical microscopy (SNOM) has attracted much interest in the past few decades since SNOM can break the diffraction limit in optical theory. Terahertz (THz) SNOM and infrared (IR) SNOM play a pivotal role in the THz/IR spectrum characterization of nanostructures and in investigating chemical molecules (chemical fingerprints). In 1928, Synge proposed the original idea of using a tiny aperture in an opaque screen

Foundation items: Supported by the National Natural Science Foundation of China (61927813, 61975225), and Science and Technology Commission of Shanghai Municipality (21DZ1101102).

Biography: Wu Changlin (1997. 12-) is a postgraduate student hailing from Longyan city, Fujian Province. He is currently pursuing a master's degree with a focus on terahertz near-field imaging. Email: clwu@mail. ustc. edu. cn.

* **Corresponding author**: E-mail: cwang@mail. sim. ac. cn, jccao@mail. sim. ac. cn

to perform near-field optical imaging. [1] Then, with the development of scanning tunneling microscopy (STM), the proposal of combining light-induced currents with near-field optical detection was presented for the study of the molecular potential. [2-3] Later, the use of the field enhancement effect of the metal tip led to the study of scattering-type scanning near-field optical microscopy (s-SNOM) [4-5] based on atomic force microscopy (AFM). In general, SNOM is based on scanning probe microscopy (SPM), and the difference lies in what kind of physical quantity is measured: the photoinduced current or far-field strength. STM-based SNOM is widely used in the THz spectrum to investigate the quantum effects of molecules. [6-8] The latest research applied hydrogen molecules as an extreme quantum sensor and achieved atomic-scale spatial and femtosecond temporal resolutions. [9] Scattering-type SNOM detects the near-field optical response through far-field demodulation, and the near-field information cannot be directly derived. As the near-field signal is submerged in a high background signal, the signal-to-noise ratio (SNR) is extremely poor, and a lock-in amplifier is often used for signal extraction. This approach relies on far-field optical quantities rather than electrical quantities and is therefore suitable for a wide range of materials, such as metals, [10] semiconductors, [11] phase change materials, [12] biological tissue, [13] low-dimensional devices [14] and graphene. [15-16] Despite the rapid progress in SNOM, the mechanism of how the electromagnetic (EM) field interacts with the tip-sample junction remains a mystery for researchers. This is a multibody scattering problem, and effects of the antenna or the length of the probe [17] and the undertip specimen size [18] deserve to be discussed.

The numerical modeling method has long been a topic of great interest for a wide range of SNOM techniques. The theory of the point dipole model (PDM), [19-20] finite dipole model (FDM), [21-22] and the lighting rod model [23] have been successful in experimental results. All the previous analytical studies have confirmed the existence of a source at the apex of the SPM probe, which works as a dipole or a monopole antenna. Recently, there has been renewed interest in using the computational electromagnetics (CEM) method for this problem. [24] Researchers can use commercial software for finite element method (FEM) calculations, finite difference time domain (FDTD) calculations and the method of moments [25] to more quantitatively calculate EM field distributions. Simulation results are used to compare analytical models. The numerical simulations help us more quantitatively study the interaction of EM fields with matter in the frequency and time domains. [24,26-28] However, increased computational degrees of freedom, such as the number of meshing grids, will prolong the computing time in each iteration, and a larger computing physical domain will require more iterations. This means that there is a dramatic increase in the iteration time step and the accumulated errors that continue to accrue. Another issue is how to demodulate the high-order harmonic signal from the background in CEM calculations. The frequency of EM waves is on the order of $10^{[12]}$, while the probe modulation frequency is on the order of 10^5. Frequencies difference is too large to directly apply simulation in the time domain. Recent investigators have examined the effects of using the dipole model on CEM simulation. [29] Such approaches, however, have failed to address the vital effects of boundary conditions, especially ignoring the role of the probe shaft. The findings of this study suggest the combination of numerical modeling methods with CEM simulation is feasible. In this paper, a physical and mathematical model is developed to provide an in-depth analysis of the formation of the charged dipole at the tip apex, and it is regarded as a near-field source in simulation. The constraints of the boundary conditions of the probe shaft are discussed and implemented in the simulation. There are many choices and designs for the probe, [30-31] and the cone probe is used in this paper as a demonstrative example of our simulation method. Further comparison is welcome and meaningful. Accurately quantifying simulation results with respect to experimental data is the ultimate goal of performing simulations. The method that directly reflects the tip-sample interaction will promote quantitative simulation research in the future.

This paper begins with analytical analysis based on Maxwell's equations, linking the concepts of dipole moments in electrodynamics, quantum mechanics, and antenna theory. It then proceeds to CEM simulation of the simplified model that regards the tip apex as a radiation source. This work aims to bridge the gap between analytical solutions and numerical simulations and to resolve the difficulties of quantitative interpretation in the theoretical analysis of SNOM. It also provides a more in-depth theoretical model for previous experimental studies and guides future experimental design.

1 Method

The theoretical calculations for this work are based on classical electrodynamics, and Maxwell's equations are analytically solved in an approximate case. The simulations are performed using commercial FEM software (COMSOL Multiphysics, RF module) to numerically solve Maxwell's equations for more realistic probe shape and sample structure. The simulation region is a $\left(\frac{4}{3}\pi 100^3\right)\ \mu\mathrm{m}^3$ sphere in which a fully matched layer spherical shell of thickness $\lambda/2$ is set up. The full domain is filled with air ($\varepsilon'_{air} = 1$), and the lower space ($z<0$) is defined as a high-resistivity silicon substrate (real part of the refractive index $n'_{air} = 3.48$) with a thickness of 10 μm (in some cases 1 μm). Gold films of certain size (from 5 nm to several μm) and thickness (10 nm, 30 nm and 50 nm) are plated on the substrate (the corresponding refractive indices are calculated using the Drude model of Au in the built-in material library). A cone is modeled in the upper space ($z>0$), keeping a sphere at the top to avoid discontinuities in the first- and second-order derivatives of Maxwell's equations. Unless otherwise specified, the probe shaft length is 15 μm, and the radius of the tip apex is $R_{tip} = 8$ nm, which is coated

with Pt (the corresponding refractive index is calculated using the Drude model of Pt in the built-in material library). In the full-wave simulation method, we directly set the incident mid-IR radiation (wavelength λ = 10 μm, frequency f = 30 THz) to a p-polarized plane wave background field, which contains only the E_z component. This background field produces no refractive reflections at the dielectric surface and contains only pure tip enhancement effects. To simplify the computational complexity of this model, we can hollow out the metallic material with Boolean operations and replace the body region with perfect electric conductor (PEC) or impedance surface boundary conditions. The mesh division is based on the internal self-grid division of COMSOL. The simulation data are postprocessed with MATLAB and plotted with Origin.

2 Analytical Description

In optical theory, the resolution of an optical system is limited by the diffraction of light waves, or Abbe's criterion. For the diffraction-limited optical microscopy system, the transverse resolution is limited by the maximum transverse wavenumber $k_{//}$, from which the bandwidth of spatial frequencies is derived as $\Delta k = 2 \cdot \mathrm{Max}(k_{\parallel}) = 4\pi N.A./\lambda$. Here, *N. A.* is the numerical aperture. Using Δx to represent the spot size, the uncertainty principle of the diffraction limit can be written as $\Delta x \Delta k = 0.61\pi$. The transverse resolution is directly limited by the wavelength λ of the detecting light. Using the de Broglie relation, the wavelength λ is given by Eq. (1).

$$\lambda = \frac{h}{p} \quad , \quad (1)$$

where h is Planck's constant, and p is the momentum of the particles. When an EM wave field is applied to a metal, photon momentum accumulation increases the electron momentum with increasing metal size, and the electron velocity rapidly increases, causing a sharp drop in the de Broglie wavelength. In other words, we could use a metal object to transform the EM wave signal into an electrical signal, which results in a dramatic improvement in the transverse resolution. This is supported by the experimental observation that the length of the metal probe and the radius of the tip affect the resolution of the measurement.

The interaction between materials and EM waves is an essential factor in modeling. When an EM wave interacts with conductive materials, such as metals or semiconductors, it causes oscillation of the electron density, which is called a plasmon. The behavior of plasmons can be described by the Drude model, where the real and imaginary parts of the complex permittivity can be written as in Eq. (2).

$$\varepsilon'(\omega) = 1 - \frac{\omega_p^2}{\omega^2+\gamma^2}$$
$$\varepsilon''(\omega) = \frac{\omega_p^2\gamma}{\omega^3+\gamma^2\omega} \quad , \quad (2)$$

where ω_p is the plasmon frequency. The plasmon frequency is related to the free electron density of the material and the effective mass of an electron: $\omega_p^2 = \frac{Ne^2}{\epsilon_0 m_e}$. By expressing the plasmon behavior through the Drude model, the reactions induced by photons and electrons inside the conducting material are expressed in the form of complex dielectric constants. We can directly write them in Maxwell's equations and simply solve the complete optical response, such as an evanescent wave, under any kind of incident EM wave. In addition, a surface plasmon (SP) occurs at the metal-dielectric interface and can propagate along the interface or be localized in the metal microstructure.[32] When a probe with a metallic surface coating is subjected to external EM excitation, an SP will be generated. Only TM waves can excite an SP, which can be theoretically explained as a collective oscillation of surface charges. The EM field irradiation excites a periodic accumulation of positive and negative charges on the surface. The tangential component of the electric field will form collective oscillation of charges and make the SP propagate along the surface. Not only does the lumpy metal surface generate an SP, but also, the accumulation of charge on the probe tip can be interpreted as an effect of the SP. The dipole source caused by the SP on the probe can help us further understand the physical mechanism of SNOM.

To depict the generation of the signal, the model also needs to consider the scanning process of SNOM. Both STM-based SNOM and AFM-based SNOM can be regarded as a tiny metal tip located above the test sample surface at a distance (d in the z-direction) scanning point-by-point in the XY plane. For example, IR/THz incident light will excite local enhancement at the tip apex, and we regard it as a dipole source in this paper. When the tip is lifted, the interaction between the enhanced local field and the sample surface will be reduced. In contrast, with decreasing tip-sample distance, even atomic-scale local field effects can be achieved [depicted in Fig. 1a]. This is a many-body problem in physics; the SPM probe, sample and substrate all contribute to the optical response. Other components also influence the field distribution, e. g. , the silicon cantilever with an aluminized coating, where the field strength at the end is also greatly enhanced [depicted in Fig. 1b; for more details, see the Supporting Information]. The light waves can incident at any angle θ, as shown in Fig. 1c, while only the z-component of the electric field contributes to the near-field enhancement. In principle, the signal generated by tip enhancement has different propagation direction and phase delay from the incident light, making it dramatically different. However, due to the diffraction limit, the spot size of the incident light is much larger than the tip apex, and only a very small amount of excitation light produces the near-field effect. This does not influence the electrical detection of STM-based SNOM. In s-SNOM detection, however, SNR of the output near-field EM signal is too small to allow direct measurement far from the tip apex. Indirect detection is necessary for s-SNOM far-field detection using a Fourier transform and similar lock-in amplifier techniques. For AFM in tapping mode, there is a displacement modulation $z(t) = A$

$(\cos 2\pi f_{tip} t + 1) + d$, where the tapping frequency f_{tip} is determined by the nature of the probe itself, but the vibration amplitude A and the distance d from the tip of the needle to the sample are controllable parameters [depicted in Fig. 1c].

The physical model is simplified by removing the cantilever of the SPM probe and replacing the tetrahedral shape of the SPM probe with an axisymmetric metal cone. This is done to avoid difficulty caused by the absence of first- and second-order derivatives of Maxwell's equations. Steep edges are also removed by reshaping the sharp lower end of the probe cone into a metal sphere with a radius of "a". This simplified model is shown in Fig. 1c. The PDM and FDM methods simplify the physical model by considering the sample to be measured as an infinite conductor and using the image method to obtain an analytical solution. The probe axis is ignored in the PDM method and replaced by the long axis of the ellipsoid in the FDM method [depicted in Fig. 1d]. The problem with this simplification is that the sample has been preset as an infinite conductor, which is not suitable for the calculation of semiconductor specimens. A more useful mathematical model is shown in Fig. 1e, which includes a z-polarized background EM field and a finite-size structure specimen. This mathematical model is suitable for investigation of STM-based SNOM, as the tip-sample junction field strength is greatly enhanced, and we can directly derive the near-field signal. However, due to the boundary conditions of the background EM field, far-field detection of tip-sample interactions is in principle indirect because of the low SNR. We, therefore, develop a mathematical model, as shown in Fig. 1f, whose boundary conditions are free propagation space. The excitation source is replaced by the dipole of the tip-sample junction, and we name it the source dipole model (SDM) method. FWS is needed to calculate the field distribution at the tip-sample junction in Fig. 1e and widely accepted in the simulation of SNOM. In this paper, the results of the simulation based on the SDM method are compared with FWS simulations.

Due to the extremely high frequency of IR/THz waves, the SPM probe can be assumed in a quasistatic state at any moment of the scan at any pixel point. In the quasistatic approximation, this problem can be simplified as a z-direction polarized electric field ($\mathbf{E} = E_0\hat{z}$) being applied to the SPM probe and the specimen below (with distance d). We then further assume that the tip-sample distance is large enough that the sample has no effect on the SPM probe; in other words, the probe is isolated from the sample. Based on these assumptions, we can analytically discuss the formation of a dipole on the tip apex.

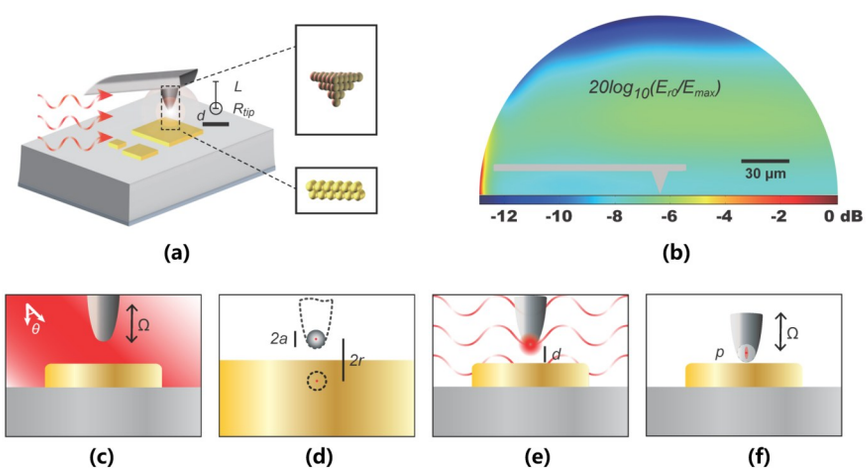

Fig. 1 Physical and mathematical modeling of s-SNOM. (a) The AFM probe works in tapping mode, with the tip-sample junction distance varying, causing strong interatomic and near-field interactions. Tip length L, radius R_{tip} and distance d is shown in (a). (b) Field distribution calculated on the sphere surface $20\lg[E(r=r_0)/\max(E)]$. Here, the maximum electric field strength is derived from the whole body simulation, (c) Full simulation model with a nonzero incident angle θ and tip tapping frequency Ω. (d) The PDM method considers the scattering tip as a polarized sphere with radius a, and the distance from the sphere center to the image sphere center is $2r$. The FDM method can be considered as replacing the sphere in the PDM method with an ellipsoid, which takes into account the effect of part of the probe shaft. (e) Use of a z-polarized background field to excite tip enhancement at the tip apex. The boundary conditions are fixed, while the tip-sample distance d is variable. (f) Dipole source model with a realistic tip shape and a fixed dipole moment; the nonlinear phenomena caused by the tip movement in tapping can be revealed in numerical computation.

图1 s-SNOM的物理和数学建模. (a) AFM探针以敲击模式工作,探针尖端与样品接触距离变化,导致强烈的原子间和近场相互作用. L为探针长度、Rtip为半径、d为探针样品距离,(b) 在球体表面上计算的场分布 20lg[E(r=r0)/max(E)];这里的最大电场强度来自于整个模拟区域,(c) 具有非零入射角θ和探针敲击频率Ω的完整模拟模型,(d) PDM方法将散射探针视为在进行振动的半径为a的球体,从球体中心到图像球体中心的距离为2r. FDM方法可以看作是将PDM中的球体替换为椭球,这样一来可以考虑到一部分探针轴的影响,(e) 使用沿Z方向极化的背景场激发探针尖端的近场增强. 边界条件固定,而探针-样品距离d可变,(f) 具有实际探针形状和固定偶极矩的源偶极子模型;在数值计算中,可以揭示由探针敲击引起的非线性现象

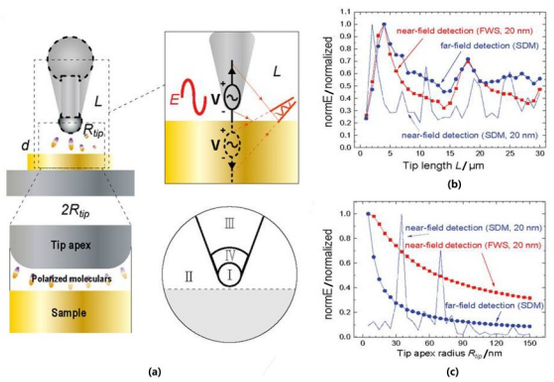

Fig. 2 Analysis of the effect of the probe shaft and tip apex on SNOM imaging, simulated with the FWS method and SDM in a 30 THz EM field. (a) Schematic diagram of the SPM probe and sample interaction. Tip length L, radius R_{tip} and distance d. The excitation of this antenna-like probe by the electric field **E** generates charge oscillations and, together with the conducting sample, forms a monopole antenna that radiates signals to the far field (top right). The capacitor equivalent to the probe tip and the sample is depicted, which generates a tunneling current due to the quantum tunneling effect. The energy state of molecules can be changed when they are filled in the gap (bottom left). For a mathematical description of the probe, the probe is divided into three regions, and a circular region is defined outside the probe (bottom right). (b) Normalized E_{near} evaluated 1 nm directly underneath the tip apex and E_{far} evaluated 2λ from the tip apex for different tip lengths L. (c) Normalized E_{near} evaluated 1 nm directly underneath the tip apex and E_{far} evaluated 2λ from the tip apex for different tip apex radii R_{tip}. Here the normE is the absolute value of the electric field strength.

图 2 在 30 THz EM 场中,利用 FWS 方法和 SDM 模拟探针轴和探针顶端对 SNOM 成像的影响分析. (a) SPM 探针与样品相互作用的示意图. 电场 E 激发了这种类似天线的探针,产生电荷振荡,并与导电样品形成单极天线,将信号辐射到远场(右上方). 探针尖端和样品等效于一个电容器,由于量子隧穿效应,探针样品结会产生隧穿电流. 当分子填充在间隙中时,能量状态会改变(左下方). 为了对探针进行数学描述,将探针分为三个区域,并在探针外定义一个圆形区域(右下方). (b) 在不同的探针长度 L 下,得到的位于距离尖端顶端 1 纳米处的归一化电场强度 Enear 和距离尖端顶端 2λ 处的归一化电场强度 Efar. (c) 在不同的探针顶端半径 Rtip 下,得到的位于距离尖端顶端 1 纳米处的归一化电场强度 Enear 和距离尖端顶端 2λ 处的归一化电场强度 Efar. 其中,normE 是电场强度的绝对值.

The signals received by s-SNOM and STM are different, but their physical interpretation can be unified [depicted in Fig. 2a]. The external excitation light, similar to an applied power source, is loaded on the probe shaft to excite oscillation of electrons and radiate EM waves. The metallic sample acts as a mirror to reflect the radiation to the far field, and it can also be regarded as an image dipole. Therefore, the tip-sample junction works as a dipole antenna consisting of an actual SPM probe dipole and a mirror dipole within the metallic sample. The most characteristic parameter is the antenna length, which usually has the strongest antenna effect at $\lambda/4$. For IR/THz light, the wavelength is often comparable to the length of the probe or even meets the conditions for the strongest antenna effect. This is why different probe lengths can result in detected signal changes in s-SNOM. [33] For nanoscale atoms in the tip-sample cavity, the probe apex can be seen as a flat metal plate. When a medium is filled between the parallel plates, changing the distance d between the two plates can change the magnitude of the field strength inside the parallel plate capacitor. Even without dielectric filling, electrons can tunnel from one metal plate to the other according to the principles of quantum mechanics. The tunneling current will be collected by a sensitive STM system and reflect the material properties at IR/THz frequencies.

Considering the probe to be isolated and using Maxwell's equations to calculate its field distribution arising under quasistatic assumptions. As depicted in the bottom right panel of Fig. 2a, the apex of the tip is a metal sphere ($R_{tip} = a$) electrically connected to a cone surface (apex angle of $2\theta_0$) and mathematically represented as in Eq. (3).

$$\begin{aligned} &\theta = \theta_0, \ if\ r > a \\ &r = a, \ if\ r \leqslant a \end{aligned} \quad , \quad (3)$$

By solving the Laplace equation $\nabla^2\Phi = 0$ (in spherical coordinates: $1/r^2\,\partial_r(r^2\partial_r\Phi) + 1/(r^2\sin\theta)\,\partial_\theta(\sin\theta\,\partial_\theta\Phi) + 1/(r^2\sin^2\theta)\,\partial_\phi{}^2\Phi = 0$), the general solution for the potential is found to be independent of ϕ due to its azimuthal symmetry, as shown in Eq. (4).

$$\Phi(r,\theta) = \sum_{n=0}^{\infty}\left[A_n r^n + B_n r^{-(n+1)}\right] P_n(\cos\theta) \quad ,(4)$$

where θ is the angle between the position vector **r** and the z-axis. A_n and B_n are parameters to be determined, and $P_n(\cos\theta)$ are Legendre polynomials in the variable $\cos\theta$. Dividing the spherical space into four zones. zones I, III, and IV are the inner part of the probe, and zone II represents the outer part. Φ_I and Φ_{II} have similar boundary conditions to those in the PDM method, and Φ_{III} must satisfy the condition that the electric field is perpendicular to the cone surface. Evidently, only one term is present: $n = 1$.

$$\begin{aligned} \Phi_I(r,\theta) &= A_1^{(1)} r\cos\theta \qquad (r \leq a) \\ \Phi_{II}(r,\theta) &= -A_1^{(2)} r\cos\theta + \frac{B_1^{(2)}}{r^2}\cos\theta \qquad (r > a \ and\ \theta > \theta_0) \\ \Phi_{III}(r,\theta) &= A_1^{(3)} r\cos\theta + \frac{B_1^{(3)}}{r^2}\cos\theta \qquad (r \gg a \ and\ \theta \leq \theta_0) \end{aligned} \quad , \quad (5)$$

Solving for the potential expression [see the Supporting Information], Φ_I and Φ_{II}, as shown in Eq. (6), are the same as the PDM results.

$$\begin{aligned} \Phi_I(r,\theta) &= -\frac{3}{\varepsilon+2}E_0 r\cos\theta \qquad (zone\ I) \\ \Phi_{II}(r,\theta) &= -E_0 r\cos\theta + \frac{\varepsilon-1}{\varepsilon+2}E_0 a^3\frac{\cos\theta}{r^2} \qquad (zone\ II) \end{aligned} \quad , \quad (6)$$

We can still equate the effect at the tip to the source dipole moment **p**. When $r \gg a$, $A_1^{(3)}$ and $B_1^{(3)}$ can be regarded as constants, and the probe potential of the larger end is

$$\Phi_{III}(r,\theta) = -\frac{1}{\varepsilon}E_0 r\cos\theta \qquad (zone\ III) \quad . \quad (7)$$

This means that the normal component of electric displacement field **D** is continuous at the end of the SPM probe and that there is no free charge. However, the potential of the probe near the tip ($r \sim a$, zone IV) is complex. Here, we approximate it based on the potential distribution in the far field,

$$\Phi_{IV}(r,\theta) = -\frac{1}{\varepsilon}E_0 r\cos\theta + \frac{\varepsilon-1}{\varepsilon(\varepsilon+2)}E_0 a^3\frac{\cos\theta}{r^2} \qquad (zone\ IV) \quad , \quad (8)$$

where the second term is the response dipole moment ($\mathbf{p}_{resp} = \mathbf{p}/\varepsilon$) induced by the effect of the source dipole on the probe. Based on the Drude model, $|\varepsilon| > 1$ and $\varepsilon < 0$ for metals. This means that the response dipole is opposite to the source dipole. The first term of Φ_{IV} is quite different from that of Φ_I, which reflects the displacement of $\mathbf{p}_{resp}$ to the origin point.

The electric field strength varies for different tip apex radii. An interesting concept is that two spheres carrying equal and opposite charges under this assumption will have different electric field strengths depending on the radius of curvature of the surface [the smaller the radius of curvature is, the stronger the electric field]. According to the uncertainty principle, the larger Δx is, the smaller Δp is. The range of the dipole moment Δp reflects the maximum amount of charge accumulated at the tip apex. Multiplying the dipole moment by the plasma oscillation frequency within the probe results in an oscillating electric dipole $\mathbf{P}(\mathbf{t}) = p\cos(\omega_p t)$ that can be related to the antenna momentum in antenna theory [see the Supporting Information].

In a word, we can establish that the SPM probe can be viewed as a dipole according to Maxwell's equations, and the role of the probe shaft cannot be ignored. This fact has been confirmed by numerous previous experiments, and this paper aims to further explore the physical mechanism of SNOM through computer simulations. As depicted in the figure, we divide the space into four regions and obtain analytical expressions for each region by utilizing various approximations. One potential approach is to increase the number of divided regions by dividing the space into smaller grids. By calculating the partial differential equations and boundary conditions satisfied at each grid point, the numerical solution of the EM field distribution in space can be obtained.

3 Simulations and results

The advantage of the analytical method is the ease and speed of calculation, but applying complex boundary conditions is difficult. The use of CEM is more suitable for describing this multibody problem with complex boundary conditions. During the modeling phase of the simulation, the metal probe can be hollowed out and replaced by impedance boundary conditions to reduce the computational cost. A perfectly matched layer (PML) boundary condition is applied outside the physical zone to avoid EM wave reflection. However, the size of the tip apex is only several nanometers, while the length of the SPM probe shaft is more than ten micrometers. The FWS method requires meshing the physical zone into millions of small mesh grids with distances less than $\lambda/6$ and extremely large computational degrees of freedom in solving. In CEM calculations, 6 components of the EM field need to be stored, and the data size is approximately 100 MB. The main challenge arises when attempting to simulate the time evolution of s-SNOM. In time domain calculations, time is considered the fourth dimension, and it must be discretized during computation, with the result of the previous time step serving as the initial condition for the next time step. This process is not only limited by the hard disk storage but also entails a cumulative error after an extremely large number of iterative calculations. The tapping mode frequency is hundreds of kilohertz, which is more than 7 orders of magnitude different from the frequency of IR/THz waves. Computing the EM field propagation more than 10^7 times in a cyclic process and expecting it to return to the original state is not reasonable. Therefore, we keep the quasistatic assumption and change the time domain calculation to a frequency domain calculation by changing the tip-sample distance d. The modulation due to the tapping process in s-SNOM can be regarded as an averaging among the signals generated at different heights.

First, the FWS and SDM methods are compared based on the results of changing the shaft length and tip apex radius. To avoid high-order harmonics calculation, FWS is only used in near-field detection of the field strength. The SDM method is suitable for far-field detection while not well fitting the near-field results. In the SNOM application, the SPM probes are always made of metal or coated with an alloy. From Eq. (8), there is almost no electric field distribution inside the metal probe. Using the impedance boundary condition instead of the entire probe body will give the same results [see the Supporting Information]. Consider the case in which only the probe is present in space. The near-field signal strength (square red symbols) is measured at a position 20 nm below the lower end of the probe, while a point two wavelengths away is selected to calculate the far-field signal (circular blue symbols). Both SDM simulation and FWS are used to compare the effects of probe shaft antenna and tip apex charge accumulation on the near-field enhancement and the strength of the far-field detected signal when changing the shaft length and tip apex radius. Different probe lengths cause an order of magnitude difference in the strength of the detected signal. A significant enhancement effect is shown for some specific probe lengths, while a linear increase in the field

strength with L is shown when L is much smaller than the IR/THz wavelength [depicted in Fig. 2b]. Increasing the tip apex radius R_{tip} will decrease the signal strength, as a larger metal structure leads to a lower charge accumulation density [depicted in Fig. 2c]. Fig. 1 also shows that the calculation of the near-field signal using the SDM method has erratic results. This occurs because by placing the dipole on a nanoscale tip apex, the mesh profile changes as the geometry changes, and the dipole as a source will enhance this difference near it.

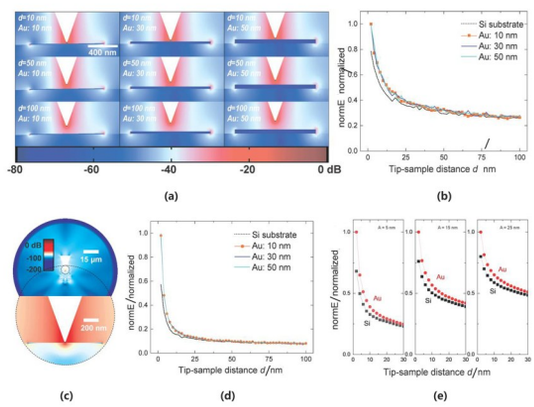

Fig. 3 Simulation application to a gold thin film. The FWS method is used to calculate the near-field enhancement with background electric field strength Ez = 3 500 V/m. (a) Spatial field distribution $20\lg[E(r)/E(d=2\text{ nm})]$ calculated for gold films of different thicknesses at different tip-sample distances d using the electric field strength 1 nm below the tip apex. The field strength at d = 2 nm is set as 0 dB, (b) Change in the normalized near-field strength 1 nm under the tip apex with increasing tip-sample distance d, as depicted in (a). (c) Whole space field distribution $20\lg[E(r)/E(d=2\text{ nm})]$ caused by the dipole source, calculated using the SDM method. The electric field strength is calculated 1 nm below the tip apex, and the field strength at d = 2 nm is set as 0 dB. (d) Change in the normalized far-field strength 1 nm under the tip apex of (c) with increasing tip-sample distance d, (e) Average far-field strength for various tapping amplitudes A; the data in (d) can be regarded as corresponding to A = 0 nm

图 3 应用于金薄膜的模拟. 使用 FWS 方法计算背景电场强度 Ez = 3 500 V/m 下的近场增强, (a)在不同的尖端-样品距离 d 和金薄膜厚度下,使用位于尖端下方 1 nm 处的电场强度计算的空间场分布 $20\lg[E(r)/E(d=2\text{ nm})]$. 并将 d = 2 nm 处的场强度设为 0 dB. (b)随着尖端-样品距离 d 的增加,(a) 中位于尖端下方 1 nm 处的归一化近场强度的变化, (c)使用 SDM 方法计算由源偶极子引起的整个空间场分布 $20\lg[E(r)/E(d=2\text{ nm})]$. 计算距离尖端下方 1 nm 处的电场强度,d = 2 nm 处的场强度设置为 0 dB, (d) 随着尖端-样品距离 d 的增加,(c) 中位于尖端下方 1 nm 处的归一化远场强度的变化, (e)探针处于不同振动幅度 A 时的平均远场强度,(d) 中的数据可以看作对应于 A = 0 nm.

We subsequently incorporated a high-resistance silicon substrate and a gold thin film into the simulations. In the FWS, the enhancement effect of the tip apex is very obvious. The enhancement effect is also observed at the edges in different gold thin films. The enhancement effect of the probe is not limited to the tip apex and extends up the probe shaft. In theory, the electric field is perpendicular to the metal surface, which means that the electric field excited by the dipole at the tip apex will propagate along the probe surface. This also avoids the physical mechanism by which the SDM can be affected by the shaft length [depicted in Fig. 2b], and the role of the dipole can be seen as a feed to the metal probe. The difference caused by the gold film thickness is not obvious in Fig. 3a. Using the FWS method for the near-field simulation, the field strength under the lower end of the probe is found to decrease as the tip-sample distance increases, which is consistent with the assumption of tip-sample capacitors [depicted in Fig. 2a]. The effect of the specimen, Si and Au on the field strength is determined by the difference in the electrical conductivity of the materials, which is reflected in the imaginary part of the dielectric constant in the optical properties. There is no background excitation in the SDM method, and the difference in tip enhancement between test samples is larger than that in the FWS results. The simulation of the near-field strength is shown in Fig. 3b for the FWS method and in Fig. 3d for the SDM method. The latter results have a larger variation with increasing d than those in Fig. 3b. This also reflects the fact that the background EM field reduces the SNR in detection, as we previously mentioned. Fig. 3b, d shows the decrease in the field strength with increasing tip-sample distance d, while the change in the field strength is small at distances greater than 30 nm. This is reflected in Eq. (6), where the tip radius a determines the decay length of the field strength. The equivalent radius of the tip apex used in the simulations is a = 8 nm. In practice, the equivalent radius is much larger due to the antenna effect, under which it can reach one magnitude enhancement. The field distribution will change with different shaft lengths and apex radii, but the trends are similar in the simulation results. [24] Common s-SNOM devices use lock-in amplifiers to demodulate the higher harmonics in tapping mode when performing far-field detection. This process extracts the far-field radiation produced by the tip enhancement effect. As the lockin amplifier extracts the sinusoidal harmonic signal of $n\omega_{AFM}$, changing the probe height brings a nonlinear effect that leads to nonsinusoidal signal production. In the simplification of this paper, the effect of the lock-in amplifier is reduced to an averaging process of the nearfield signal produced by the radiation field at different vibrational positions. The change in the far-field signal is measured for different amplitudes A in tapping mode, as depicted in Fig. 3e. An increase in A increases the background component of the signal while reducing the variability in the far-field signal generated by different samples. Compared to the studies that use Fourier transformation to obtain the far-field signal, [24] the SDM method can directly link the far-field and near-field results, more realistically reflecting the connection between them.

At the end of this paper, we employ CEM calculations to simulate the tip-sample scanning process and convert the electrical field strength into a grayscale pixel image. The scanning process is mechanically driven by a piezoelectric transducer (PZT) to displace the sample

stage, which in turn gives optical information at each sampling point. During the simulation, the position of the probe changes, which is equivalent to moving the sample stage. The discrete movement of the probe is called a step; here, the step distance is set to 50 nm, and a line scan is obtained in the X direction, followed by stepping in the Y direction until the entire sample of 1 μm × 1 μm has been scanned. The previous simulation results show that the thickness of the metal thin film has little effect on the optical signal, and we will now discuss the influences of the lateral sample size. The isolated Au sample exhibits a similar tip enhancement to the SPM probe at small sizes. As the sample size increases, the enhancement effect of the Au sample decreases. When the size of the metal sample is comparable to the tip apex radius, this setup can be regarded as a tip-sample cavity or a small plate capacitor. As the sample width further increases, more source dipole radiation will interact with the sample, resulting in a larger detected field strength. When the sample width is much larger than the tip-sample cavity interface, increasing the sample size no longer has a significant effect. For the Au sample connected to outside metals, the entire connected sample forms an antenna structure, similar to two metal spheres of different sizes joined together. When the source dipole radiates at the ground (the larger sphere), the result is similar to the situation of measuring an infinite metal plate. Because the sample (the smaller sphere) is electrically connected to the larger sphere, more charge will accumulate on the smaller sphere, enhancing the field strength. In other words, antenna effects produce a higher detected signal of the connected specimen. The simulation results show that the turning point for changing sample size occurs at W_{sample} ~ 50 nm, the same as the gold film thickness. In Fig. 4b, the field strength in the FWS calculation is also related to the sample size and the free charge amount. The grounded Au sample can transport charges from peripheral metal, resulting in a higher surface charge density than for the ungrounded Au sample. More surface charges will reflect more electromagnetic waves to the far field, resulting in a small field strength near the surface. With increasing sample width, the field strength of isolated and connected metals gradually becomes steady because the field enhancement is limited to near the tip apex. In the SDM calculation, the source dipole radiates on the metal surface with a constant strength. Isolated metal acts as a mirror dipole, reflecting more signal to the far field with increasing sample size, and the result is similar to that of FWS. In the SDM method, connected small metal works like an antenna in the simulation. When the impedances of the source dipole and connected metal match (here, $W_s = d$), the connected metal absorbs more electric energy and reflects less to the far field. This phenomenon could not be discovered in the FWS because the metal sample will influence the tip apex enhancement as feedback. Further verification through experiments will help explain this phenomenon. After scanning the sample in the simulation and converting the near-field E_z signal to a grayscale plot (Fig. 4c), the field strength of the connected samples can more clearly be observed to increase as the sample becomes larger. For the isolated samples, the signal intensity remains almost constant. A similar experiment verified this phenomenon for gold in the THz range. [10,18,34] Gold in the THz range is highly reflective and could be simplified to a PEC. The application of imaging simulation to the structures of other materials in the mid-infrared band is a research direction that can be pursued in the future. [25] At the end of this paper, we further bridge the analytical description and the simulation through a discussion of the resolution. Resolution is an important index of the quality of an image. From Eq. (6), the first-order differential of the potential is the electric field strength, and the SNOM resolution can be considered to be the tip apex radius. In Fig. 4c, the tip-sample distance and scanning step are 50 nm, which means that the resolution in constructing the grayscale image will not be better than 50 nm. However, the electric field is not local, and we can faintly see the 10 nm wire in the grayscale plot, which suggests that the actual resolution of the simulated image is still ultimately determined by the tip apex radius.

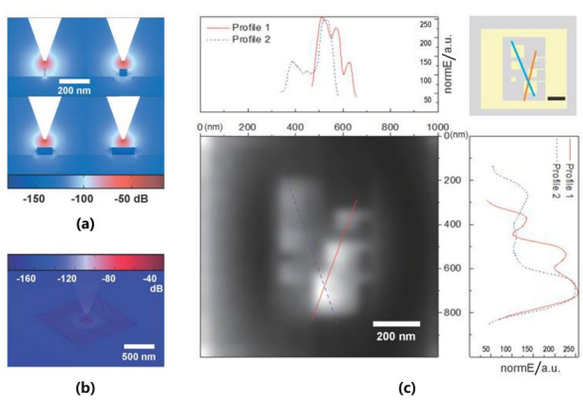

Fig. 4 Simulation of the difference between near-field and far-field signals for Au samples of different sizes, grounded or not (connected to a larger metal is considered grounded). (a) The electric field distribution around the 50 nm thick gold samples is calculated at d = 50 nm. Let the electric field strength at 2 nm from apex for the 1 nm wide sample be 0 dB. (b) 3D distribution of electric field strength for an isolated Au sample, (c) Simulated imaging of a sample with grounded and ungrounded gold square patches (narrowest line width of 10 nm), with a step size of 50 nm in (X, Y) scanning. Top view of the sample (top right; for details, see the Supporting Information). Grayscale plot of the near-field Ez signal (bottom left, 1 000 nm × 1 000 nm). The top left and bottom right are the electric field strength distributions corresponding to the two profile lines with 256 as the maximum value, respectively

图4 模拟不同大小、接地或未接地(连接到较大金属被视为接地)时,Au样品近场和远场信号的差异,(a) d=50 nm时金样品周围的电场分布,计算中设1 nm宽的样品在离探针尖端2 nm处的电场强度为0 dB,(b) 孤立未接地Au样品的电场强度的三维分布,(c) 模拟接地和未接地正方形金片样品(最窄线宽为10 nm)的成像,步长为50 nm的(X,Y)扫描. 样品的俯视图(右上角;详见支持信息);近场Ez信号的灰度图(左下,1 000 nm×1 000 nm),其最大值为256;左上和右下分别是对应于最大值为256的两条轮廓线的电场强度分布

4 Conclusion

In conclusion, the SDM method has been successfully applied in FEM simulation. Through mathematical analysis, we have confirmed that the combination of the tip apex radius and probe shaft contributes to the formation of the dipole at the tip apex. By employing the FWS and SDM methods, we have investigated the distributions of the near-field strength and far-field strength, and analyzed the effects of varying thicknesses and sizes of samples on the detected field strength. Furthermore, we have discussed the factors that affect the resolution and contrast of SNOM imaging. One of the objectives of this project is to develop an efficient CEM simulation method that is compatible with IR/THz s-SNOM, which can be used in future comparative studies with experimentally obtained images. Moreover, this paper demonstrates how to calculate a near-field image via simulation. The complex sample structure justifies a full image simulation, which can reveal local enhancement from the small structures. Using more pixels in the image simulation can lead to higher sensitivity. In the future, our approach can be extended to a more quantitative study of nanometer optical properties based on experimental data.

Acknowledgment

One of the authors (C. L. W) would like to acknowledge valuable support and discussions from Wen Guan and Chenjie Wang.

References

[1] Synge E H. A suggested method for extending microscopic resolution into the ultra-microscopic region [J]. *The London Edinburgh and Dublin Philosophical Magazine and Journal of Science*, 1928, **6**: 356-362.
[2] Wessel J. Surface-enhanced optical microscopy [J]. *Journal of the Optical Society of America B*, 1985, **2**: 1538-1541.
[3] Williams C C, Wickramasinghe H K. Microscopy of chemical-potential variations on an atomic scale[J]. *Nature*, 1990, **344**: 317-319.
[4] Novotny L, Sánchez E J, Xie X S. Near-Field Optical Imaging Using Metal Tips Illuminated by Higher-Order Hermite-Gaussian Beams [J]. *Ultramicroscopy*, 1998, **71**(1): 21-29.
[5] Hillenbrand R, Taubner T, Keilmann F. Phonon-enhanced light-matter interaction at the nanometre scale [J]. *Nature*, 2002, **418**: 159-162.
[6] Cocker T L, Jelic V, Gupta M, *et al*. An ultrafast terahertz scanning tunnelling microscope[J]. *Nature Photonics*, 2013, **7**(8):620-625.
[7] Neuman T, Ruben E, Casanova D, *et al*. Coupling of Molecular Emitters and Plasmonic Cavities beyond the Point-Dipole Approximation[J]. *Nano Letters*, 2018, **18**(8):2358-2364.
[8] Wagner C, Green M F B, Maiworm M, *et al*. Quantitative imaging of electric surface potentials with single-atom sensitivity [J]. *Nature Materials*, 2019, **18**: 853-859.
[9] Wang L, Xia Y, Ho W. Atomic-scale quantum sensing based on the ultrafast coherence of an H_2 molecule in an STM cavity[J]. *Science*, 2022, **376**: 401-405.
[10] Pizzuto A, Chen X, Hu H, *et al*. Anomalous contrast in broadband THz near-field imaging of gold microstructures [J]. *Optics Express*, 2021, **29**: 15190-15198.
[11] Von Ribbeck H -G, Brehm M, Van der Weide D, *et al*. Spectroscopic THz near-field microscope [J]. *Optics Express*, 2008, **16**: 3430-3438.
[12] Nishida J, Johnson S C, Chang P T, *et al*. Ultrafast infrared nanoimaging of far-from-equilibrium carrier and vibrational dynamics [J]. *Nature Communications*, 2022, **3**: 1 - 9.
[13] Yang Z, Tang D, Hu J, *et al*. Near-Field Nanoscopic Terahertz Imaging of Single Proteins[J]. *Small*, 2021, **17**(3): 2005814.
[14] Eisele M, Cocker T L, Huber M A, *et al*. Ultrafast multi-terahertz nano-spectroscopy with sub-cycle temporal resolution. *Nature Photonics*, 2014, **8**: 841 - 845.
[15] Fei Z, Andreev G O, Bao W, *et al*. Infrared nanoscopy of Dirac plasmons at the graphene-SiO_2 interface [J]. *Nano Letters*, 2011, **11**(11):4701-4705.
[16] Alonso-González P, Nikitin A Y, Gao Y, *et al*. Acoustic terahertz graphene plasmons revealed by photocurrent nanoscopy [J]. *Nature Nanotechnology*, 2016, **12**: 31-35.
[17] Huth F, Chuvilin A, Schnell M, *et al*. Resonant Antenna Probes for Tip-Enhanced Infrared Near-Field Microscopy [J]. *Nano Letters*, 2013, **13**(3):1065-1072.
[18] Chen X, Liu X, Guo X, *et al*. THz Near-Field Imaging of Extreme Subwavelength Metal Structures [J]. *ACS Photonics*, 2020, **7**: 687-694.
[19] Knoll B, Keilmann F. Enhanced dielectric contrast in scattering-type scanning near-field optical microscopy [J]. *Optics Communications*, 2000, **182**:321-328.
[20] Keilmann F, Hillenbrand R. Near-field microscopy by elastic light scattering from a tip. *Philosophical Transactions of the Royal Society of London. Series A: Mathematical, Physical and Engineering Sciences*, 2004, **362**: 787 - 805.
[21] Cvitkovic A, Ocelic N, Hillenbrand R. Analytical model for quantitative prediction of material contrasts in scattering-type near-field optical microscopy[J].*Optics Express*, 2007, **15**(14): 8550-8565.
[22] Govyadinov A A, Amenabar I, Huth F, *et al*. Quantitative Measurement of Local Infrared Absorption and Dielectric Function with Tip-Enhanced Near-Field Microscopy [J]. *Journal of Physical Chemistry Letters*, 2013, **4**(9): 1526-1531.
[23] Mcleod A S, Kelly P, Goldflam M D, *et al*. Model for quantitative tip-enhanced spectroscopy and the extraction of nanoscale-resolved optical constants[J]. *Physical Review B*, 2014, **90**(8): 085136.
[24] Mooshammer F, Huber M A, Sandner F, *et al*. Quantifying nanoscale electromagnetic fields in near-field microscopy by Fourier demodulation analysis[J]. *ACS Photonics*, 2020, **7**: 344-351.
[25] McArdle P, Lahneman D J, Biswas A, *et al*. Near-field infrared nano-spectroscopy of surface phonon-polariton resonances. *Physical Review Research*, 2020, 2: 023272.
[26] Hillenbrand R. Infrared and terahertz nanoscopy for dielectric imaging and near-field mapping of antennas and transmission-lines. *2011 International Conference on Infrared, Millimeter, and Terahertz Waves*, 2011: 1 - 3.
[27] Chen X, Lo C F B, Zheng W, *et al*. Rigorous numerical modeling of scattering-type scanning near-field optical microscopy and spectroscopy[J]. *Applied Physics Letters*, 2017, **111**(22): 223110.
[28] Mastel S, Govyadinov A A, Maissen C, *et al*. Understanding the image contrast of material boundaries in IR nanoscopy reaching 5 nm spatial resolution[J]. *ACS Photonics*, 2018, **5**: 3372-3378.
[29] Feres F H, Mayer R A, Wehmeier L, *et al*. Sub-diffractional cavity modes of terahertz hyperbolic phonon polaritons in tin oxide[J]. *Nature Communications*, 2021, **12**(1): 1-9.
[30] Thomas L, Hannotte T, Santos C N, *et al*. Imaging of THz Photonic Modes by Scattering Scanning Near-Field Optical Microscopy [J]. *ACS Applied Materials & Interfaces*, 2022, **14**: 32608-32617.
[31] Zhang Y, Chen X, Chen D, *et al*. Partially Metal-Coated Tips for Near-Field Nanospectroscopy [J]. *Physical Review Applied*, 2021, **15**: 014048.
[32] Hecht B, Bielefeldt H, Novotny L, *et al*. Local Excitation, Scattering, and Interference of Surface Plasmons [J]. *Physical Review Letters*, 1996, **77**(9):1889-1892.
[33] Mastel S, Lundeberg M B, Alonso-González P, *et al*. Terahertz Nanofocusing with Cantilevered Terahertz-Resonant Antenna Tips [J]. *Nano Letters*, 2017, **17**(11): 6526-6533.
[34] Zhang W, Chen Y. Visibility of subsurface nanostructures in scattering-type scanning near-field optical microscopy imaging [J]. *Optics Express*, 2020, **28**(5): 6696.